Petroleum Science 22 (2025) 4794–4808

Contents lists available at ScienceDirect

Petroleum Science

journal homepage: www.keaipublishing.com/en/journals/petroleum-science

Original Paper

Development and feasibility test of a fan-shaped hydrate simulator with a radius of 3 m

Ling-Ban Wang [a,1], Xiao-Hui Wang [a,1], Yu-Hao Bu [a], Zhen-Bin Xu [a], Xian Sun [a], Yi-Fei Sun [a,*], Peng Xiao [a], Qing-Ping Li [b], Shou-Wei Zhou [b], Praveen Linga [c], Chang-Yu Sun [a,b,**], Guang-Jin Chen [a,***]

[a] State Key Laboratory of Heavy Oil Processing, China University of Petroleum (Beijing), Beijing 102249, China
[b] Fundamental and Frontier Research Center, Huairou Laboratory, Beijing 101400, China
[c] Department of Chemical and Biomolecular Engineering, National University of Singapore, Singapore 117582, Singapore

ARTICLE INFO

Article history:
Received 21 February 2025
Received in revised form
16 June 2025
Accepted 9 October 2025
Available online 13 October 2025

Edited by Min Li

Keywords:
Methane hydrate
Fan column-shaped simulator
Joint detection method
Production behavior
Multi-field evolution

ABSTRACT

Large-scale physical simulation is essential for advancing our understanding of natural gas hydrates exploitation mechanism. However, cylinder-shaped simulators often face challenges in balancing large volume, controllability, and comprehensive monitoring. In this study, we developed a fan column-shaped hydrate simulator (FCHS) with an internal angle of 6°, a radius of 3 m, and an inner height of 0.3 m, resulting in an effective volume of ~142 L. Moreover, the FCHS is equipped with an integrated "thermal-pressure-acoustic" sensing system, enabling in-situ monitoring of temperature, pressure, and P-wave velocity evolution during hydrate formation and dissociation process. The experimental results indicate that a pressure gradient successfully established from the reservoir center toward its boundaries during depressurization stage, and pressure propagation is relatively slow, resulting in a radial pressure difference of 3–4 MPa within a 3 m range. Once the system reaches pressure equilibrium, the pressure difference decreases to 0.3–0.4 MPa. The depressurization at the wellbore promotes hydrate dissociation in the near-well region, resulting in the radial temperature difference reaches ~1.5 °C along the radial direction. The acoustic data reveals that a radial gradient in hydrate saturation gradually forms from the center to the boundary during depressurization-induced gas production. The evolutions of spatio-temporal multi-fields obtained in the FCHS are consist with that of field production. The FCHS proves to be a cutting-edge platform for experimental simulation of NGH exploitation and carbon sequestration processes.

1. Introduction

Natural gas hydrates (NGHs), commonly referred to as combustible ice, is a crystalline compound where water molecules form cages containing gas molecules. Recognized for its vast methane reserves, NGHs have garnered significant global attention from academic and industrial sectors (Boswell et al., 2011; Demirbas, 2010; Milkov et al., 2002; Yin et al., 2019). Over 95% of known NGH reserves are found in unconsolidated sediments of deep and shallow seafloors, presenting substantial potential for commercial exploitation (Feng et al., 2021). Many countries and regions have conducted extensive technical studies to develop these resources with the goal of commercial exploitation (Liu et al., 2015, 2022; Lu et al., 2011; Xu et al., 2022).

Due to the high cost of field production tests for marine NGHs and the fact that factors affecting gas production behaviors vary with reservoir scale (Tang et al., 2007), there is a growing consensus in research to develop large-scale experimental hydrate simulators that can realistically simulate NGH exploitation processes. Several three-dimensional experimental systems have been established for synthesizing hydrate-bearing sediments (HBS) samples, such as PHS (pilot-scale hydrate simulator, Φ

* Corresponding author.
** Corresponding author.
*** Corresponding author.
E-mail addresses: sun.yifei@cup.edu.cn (Y.-F. Sun), cysun@cup.edu.cn (C.-Y. Sun), gjchen@cup.edu.cn (G.-J. Chen).
Peer review under the responsibility of China University of Petroleum (Beijing).
[1] These authors contributed equally to this work.

https://doi.org/10.1016/j.petsci.2025.10.003

0.5 m × 0.6 m, 117.8 L) (Li et al., 2012b, 2012c; Wang et al., 2013), TDHS (three-dimensional hydrate simulator, Φ 0.5 m × 1.0 m, 196 L) (Li et al., 2018b, 2021; Su et al., 2012a; Wang et al., 2020), LARS (large-scale laboratory reservoir simulator, Φ 0.46 m × 1.3 m, 210 L) (Heeschen et al., 2016; Priegnitz et al., 2013; Schicks et al., 2011, 2013), FLYS (field-like hydrate system, Φ 0.6 m × 1.0 m, 282.6 L) (Huang et al., 2023; Liu et al., 2020), HIGUMA (high-pressure giant unit for methane hydrate analysis, Φ 1.0 m × 1.0 m, 810 L) (Nagao, 2012), and LHRS (large-scale hydrate recovery simulator, Φ 1.2 m × 1.5 m, 1600 L) (Ge et al., 2023). Notably, the volumes of LARS, FLYS, and HIGUMA listed here deviate from the publicly reported values due to the exclusive consideration of the volume associated with the HBS sample container section. In general, the simulation scale of the aforementioned experimental apparatus with a large volume remains insufficient. Even for the LHRS, which has the largest effective volume, if the simulated production well is positioned along the central axis of the simulator, the radius of simulated sediments around the well only reaches 0.6 m. This presents challenges in establishing a representative radial pressure gradient during the hydrate production process and even causes the hydrate distributed near the wall of the high-pressure reactor to preferentially dissociate, highlighting the necessity for the development of larger-scale hydrate simulators.

The popular approach applied to construct large-scale hydrate simulators typically involves scaling up cylinder-shaped high-pressure vessels by increasing both their radius and height. However, conventional methods encounter significant challenges when addressing larger-dimensional scenarios. Firstly, scaling up a conventional cylinder-shaped hydrate simulator leads to a significant increase in volume; for instance, the volume of a cylinder-shaped simulator with a diameter and height of 1 m is 785 L, whereas it escalates to 170,000 L when both dimensions are increased to 6 m. To simulate the marine high-pressure conditions conducive to the stable existence of hydrates, the apparatus must be designed to operate at pressures exceeding 30 MPa. These factors contribute to the insurmountable difficulties faced by materials and manufacturing processes. Even if it is successfully developed, the operational challenges present formidable obstacles, including substantial material and energy consumption, safety concerns, high operational costs, and time-wasting associated with preparing HBS samples. In response to the bottlenecks encountered in the manufacturing and operation of pilot-level hydrate simulators, a novel design philosophy featuring a fan column-shaped structure is introduced, establishing an equivalent simulation method tailored for large-scale applications at a reduced volume. The new apparatus effectively simulates diameters of up to 6 m, which is significantly larger than that of existing large-scale hydrate simulators. This undoubtedly represents a significant breakthrough in advancing the physical simulation of NGHs development.

2. Design philosophy

During the field exploitation of NGHs, each well impacts a disk-shaped area with a radius ranging from tens to hundreds of meters, as shown in Fig. 1. Ignoring reservoir heterogeneity leads to an axisymmetric distribution of various physical fields around the vertical production well. Therefore, by analyzing the multi-field structure within a fan column-shaped geological body at a specific azimuth, the relevant results can be extrapolated to the entire reservoir, irrespective of its size. Furthermore, to reduce grid count and save computational, many numerical simulations also often utilize the axisymmetric characteristics to divide grids only within a smaller azimuthal angle.

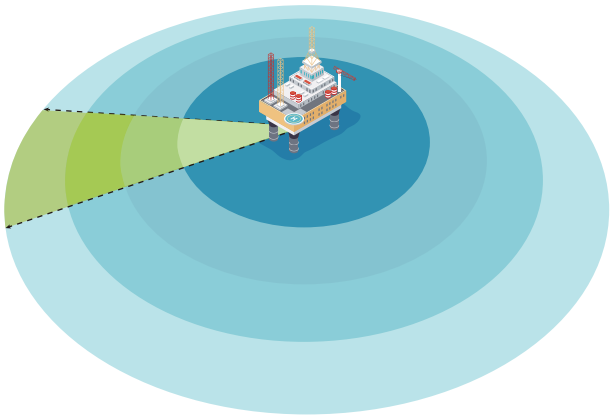

Fig. 1. Aerial view of the affected areas of vertical production well.

Inspired by these considerations, a fan column-shaped hydrate simulator (FCHS) was developed to balance volume and scale efficiency, as shown in Fig. 2. The FCHS features a large radius and moderate internal height, enabling it to simulate production processes across extensive spatio-temporal scales effectively. This novel design ensures that the sediment volume remains manageable, thereby reducing manufacturing costs while improving operational timeliness and safety. Moreover, its configuration is well-aligned with the reservoir domain used in numerical simulation studies, which facilitates cross-validation between experimental results and numerical simulations. This alignment enhances the applicability of the results to real-world scenarios. Therefore, the FCHS will serve as a cutting-edge platform for simulating the NGH exploitation and marine CO_2 sequestration in the form of solid hydrates.

3. Experimental system

Fig. 3 presents a photograph and a schematic diagram of the entire experimental system, which is divided into two primary sections. The 1st section is dedicated to the formation of HBS samples, including a high-pressure vessel, an in-situ detection and data acquisition system, a temperature control system, and a material supply system. The 2nd section focuses on the dissociation of HBS samples and fluid production, including a production and collection system as well as a safety system.

3.1. High-pressure reactor

The FCHS, manufactured by Jiangsu Coraland Machinery, showcases key design and manufacturing innovations for an unconventional fan column-shaped high-pressure vessel. As illustrated in Fig. 4, the vessel addresses challenges such as localized stress concentration and sealing through a combination of "static-seal" and "dynamic-seal" solutions.

The fan-column cavity was machined from a trapezoidal stainless-steel forging with a rounded top angle to reduce stress concentration. A trapezoidal forging serves as the sealing cover, ensuring effective welding and sealing of the cavity (static seal). Circular flange holes were added to the sealing cover and bottom for external communication and resealing (dynamic seal). This combination of static and dynamic seals effectively addresses the sealing challenges associated with the unconventional high-pressure vessel. Finally, constructed from SUS316L stainless steel, the FCHS features a 6° internal angle, a 3 m radius, an inner height of 0.3 m, a maximum volume of 142 L, and a design pressure of

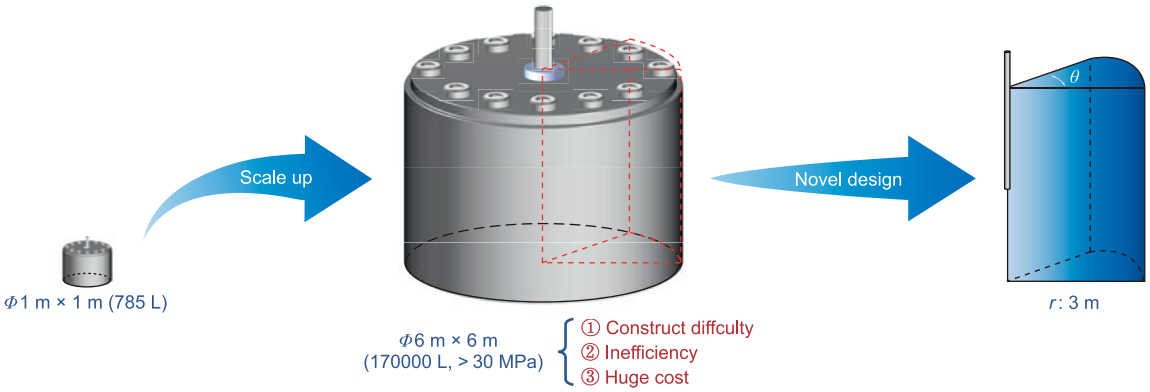

Fig. 2. Design philosophy of the fan column-shaped hydrate simulator.

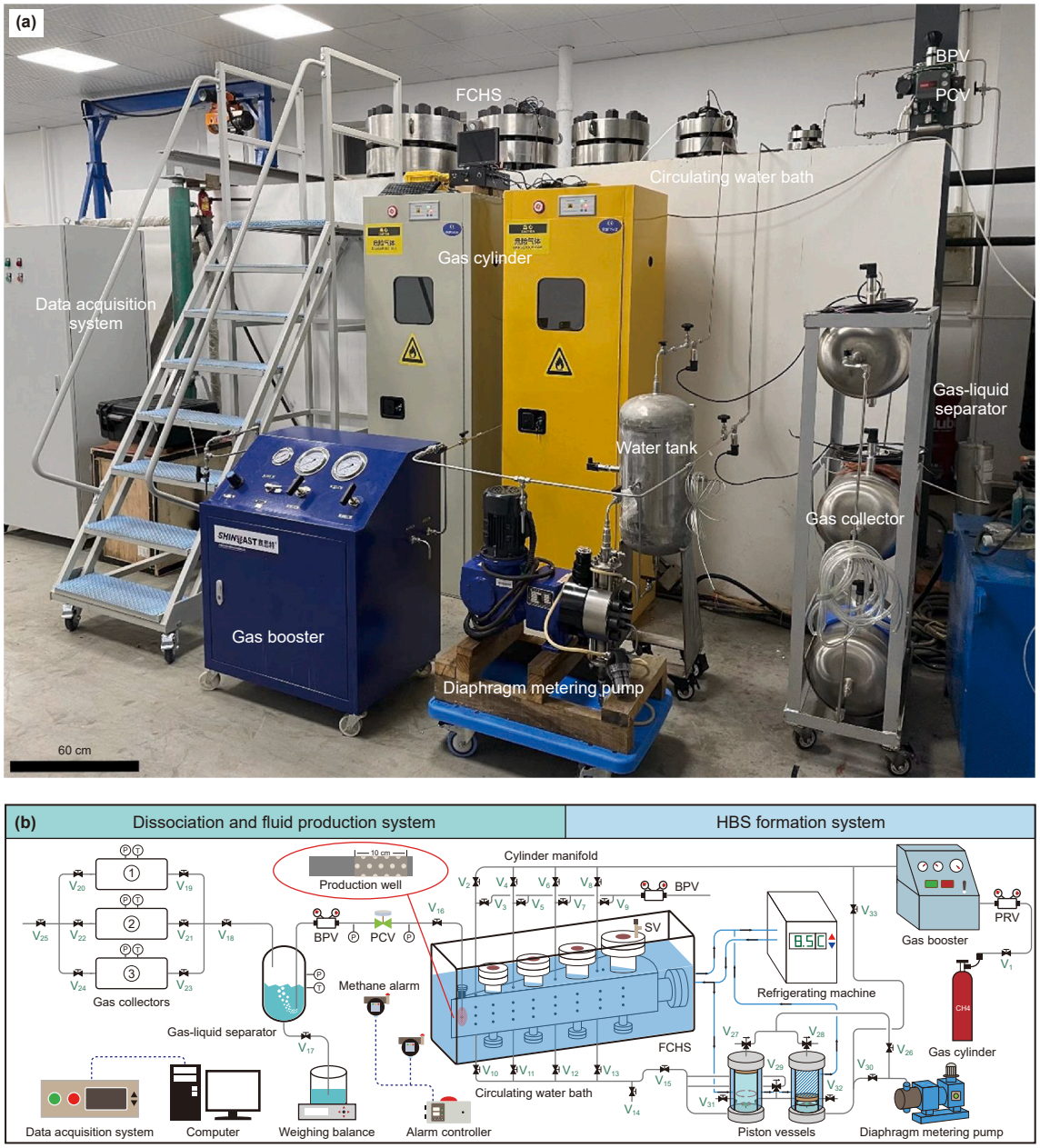

Fig. 3. Experimental system established around the FCHS: **(a)** actual picture and **(b)** schematic diagram.

Fig. 4. The fan column-shaped hydrate simulator.

30 MPa. For a fan column-shaped simulator with a radius of 3 m and an inner height of 0.3 m, the narrow-end tip becomes a site of stress concentration. Finite element analysis indicated that the internal angle must exceed 5° to maintain mechanical integrity under the design pressure of 30 MPa. An internal angle of 6° was thus selected, as it not only meets safety requirements but also evenly divides 360°. On the other hand, if the internal angle exceeds 6°, the manufacturing cost of the apparatus will increase significantly. For instance, an increment of just 1° in internal angle may increase manufacturing costs by hundreds of thousands. Therefore, 6° was chosen as the optimal compromise between structural safety, experimental scalability, and cost-effectiveness. Based on the principle of equivalent extension, the experimental results obtained can be scaled up to a simulated reservoir with a volume of ~8520 L.

As shown in Fig. 4, the vessel exterior features eleven welded flanges, and the purpose of each flange is marked. Specifically, four pairs of opposing flanges positioned radially on the upper and lower surfaces are used for the installation of the ultrasonic probe. For potential axial extension, the internal diameter of the upper five flanges varies with the vessel's central width, thereby ensuring consistency with the internal dimensions. To prevent overpressure during experiments, a safety valve (SV) (SS-418B5, Xiongchuan Valve) was installed at the largest upper flange. A flange positioned nearest the top enables the installation of a production well, enhancing flexibility for pipeline replacement, while a flange located on the curved lateral side facilitates sand-packing. Additionally, threaded operational holes on the upper, lower, and lateral surfaces permit the installation of pipelines, temperature sensors, and pressure transducers. For minimizing tangential heat transfer, asbestos insulation is applied to the planar sidewalls (parallel to the radial direction). In contrast, the arcuate surfaces, as well as the top and bottom plates, are left uninsulated, serving as the primary heat exchange interfaces during hydrate production.

The FCHS was mounted on a rotatable bracket around a fixed shaft and can be rotated to a specific angle using a hydraulic elevator. This design greatly enhances the efficiency of the sand-packing process, which will be discussed in detail in the subsequent sections.

3.2. Pressure measurement unit

The effective range of depressurization is pivotal in field tests, with pressure propagation analysis contributing to the optimization of production technologies. In this unit, 17 pressure transducers (KLXT-KO-HAG, Beijing Collihigh Sensing Technology) were positioned to establish pressure fields during the experiments.

As shown in Fig. 5, there are three distinct pressure measurement planes. The central plane hosts nine transducers aligned along its axis, while the upper and lower planes each contains four transducers. To avoid measuring wall pressure, all transducers were connected to the sediment interior through pre-set pipelines. The designations UP_i (upper plane), MP_i (middle plane), and LP_i (lower plane) specify the positions of transducers on each plane. Pressure data were collected using a monitor and control generated system (MCGS, Beijing Collihigh Sensing Technology).

3.3. Temperature measurement unit

The thermal variation of HBS is closely linked to production behaviors. To gain a comprehensive insight into the temperature field variations, 18 temperature sensors with 42 temperature measurement points (JWB/PT100/C, Beijing Collihigh Sensing Technology) were inserted into the sediments, as shown in Fig. 6.

Nine vertical planes (VP) were divided for temperature measurement, with distances ranging from 120 to 2720 mm. For regions within 820 mm, a single point is sufficient; however, for regions beyond 820 mm, three points are used to enhance accuracy. These points are uniformly designated as UT_i for the upper horizontal plane and LT_i for the lower horizontal plane. For instance, in VP_9, there are six measurement points: UT_{19}, UT_{20}, and UT_{21} for the upper plane, and LT_{19}, LT_{20}, and LT_{21} for the lower plane. The MCGS was used to collect temperature data.

3.4. P-wave measurement unit

Ensuring the safety and controllability of the commercial exploitation of NGHs requires a comprehensive understanding of the mechanical properties of HBS during production. Notably, the degree of reservoir consolidation is closely related to hydrate saturation (S_H), and its evolution can be inferred through P-wave velocity (V_P) measurements. As illustrated in Fig. 7, to access S_H in situ, four pairs of ultrasonic probes (TGM-CJ, Hunan Tiangong Measurement & Control Technology) were positioned radially, with the measured values designated as V_{P1-4} in sequence. An acoustic parameter tester (TH204, Hunan Tiangong Measurement & Control Technology) was used to analyze and record V_P data.

3.5. Temperature control system

To replicate realistic geological conditions, the FCHS was immersed in a water tank maintained by a constant-temperature water bath. Fig. 8 presents both actual photographs and a schematic diagram of the system. Six multi-point temperature sensors were strategically placed in the water tank: four at the corners and two on either side of the vessel. To enhance heat dissipation, an outdoor refrigeration unit (NLPA-10.1, NULE CHILLER) was employed. This system features energy efficiency, high accuracy (±0.2 °C fluctuation), uniform temperature distribution, broad adjustability, and the capability for extended continuous operation.

3.6. Material supply and production system

High-pressure gas was delivered using a gas cylinder and a gas booster (GBS-STCD25, Jinan Shineeast Fluid Systems Equipment), with the intake pressure regulated by a pressure-reducing valve (PRV) (SS-88402-8F-2P, Xiongchuan Valve). The preparation and

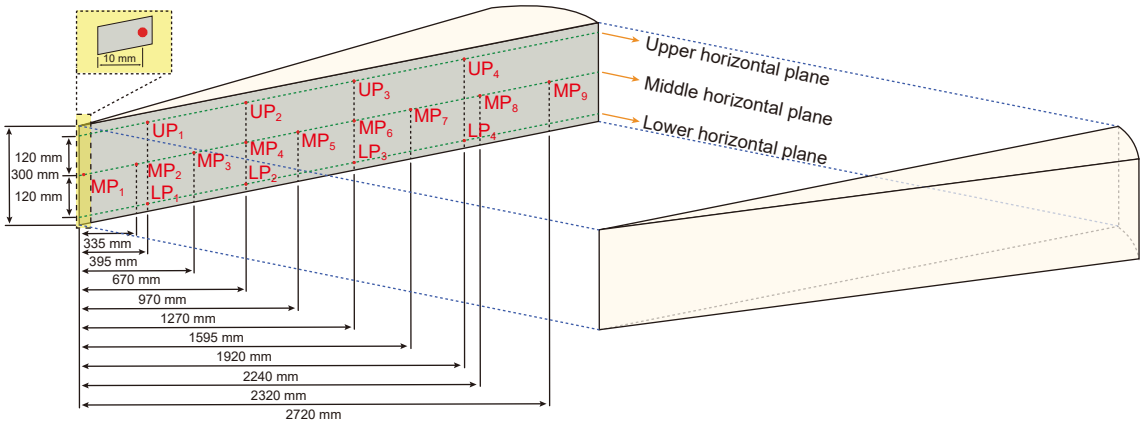

Fig. 5. Schematic diagram of the pressure measurement points.

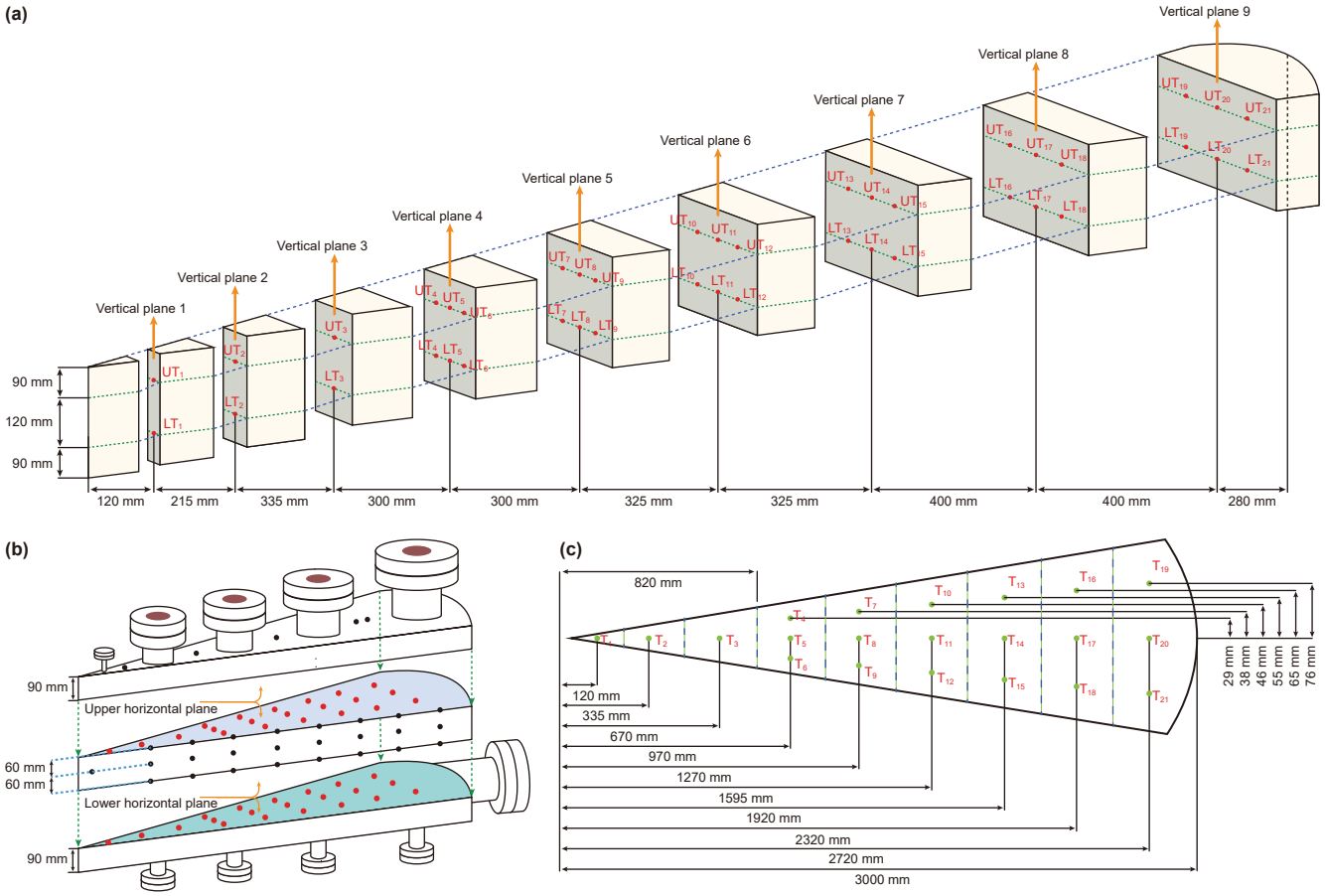

Fig. 6. Schematic diagram of the temperature measurement points for **(a)** nine vertical planes, **(b)** two horizontal planes and **(c)** a horizontal plane.

delivery of various liquids or emulsions were used by a diaphragm metering pump (DMP) (SJ2-M-10/15, SBPUMP) and a piston vessel (Jiangsu Huaan Scientific Research Devices) equipped with a stirring function. For hydrate production, the system consists of a production well, a pneumatic control valve (PCV) (Series 24000SB, FISHER), a back-pressure valve (BPV) (SS-K9138N-2P, XIONGCHUAN VALVE), a gas-liquid separator, and gas collectors. The production well, featuring an opening section of ~10 cm, was wrapped with screen mesh for sand control. Flow rate regulation was achieved using the PCV, wherein a PID-controlled positioner adjusts the valve opening degree. A BPV, positioned downstream of the outlet, was pre-set to the desired production pressure (P_{prod}). Produced fluids were separated in a 4 L gas-liquid separator (Jiangsu Huaan Scientific Research Devices). The separated gas was stored in multiple 25.4 L gas collectors, while the brine was periodically measured using a weighing balance. Pictures of the aforementioned components are provided in Fig. S2 in the Supporting Information.

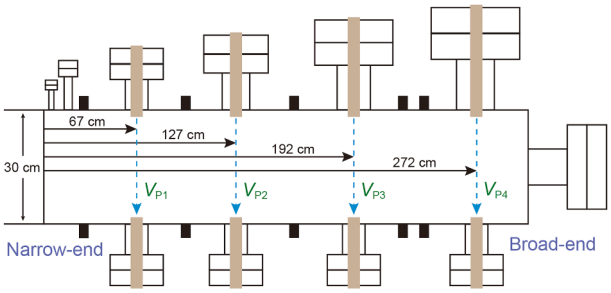

Fig. 7. Schematic diagram of the P-wave measurement points.

Initial inclination: The broad-end of the vessel was elevated by ~10° using a flip bracket and hydraulic elevator, allowing a sand-brine mixture (mass ratio ~5:1) to occupy ~70% of the cavity.

Horizontal loading: The vessel was leveled, and the mixture was introduced through four upper flanges. Due to poor fluidity, local accumulations, referred to as "hills", formed beneath the openings, necessitating a transition to the next step.

Brine-assisted redistribution: The vessel was inclined again (~10°), with brine injected through the largest upper flange and drained through a lower port at the narrow-end. A filter at the drainage port retained the mixture within the vessel. This step typically lasts 1–2 h.

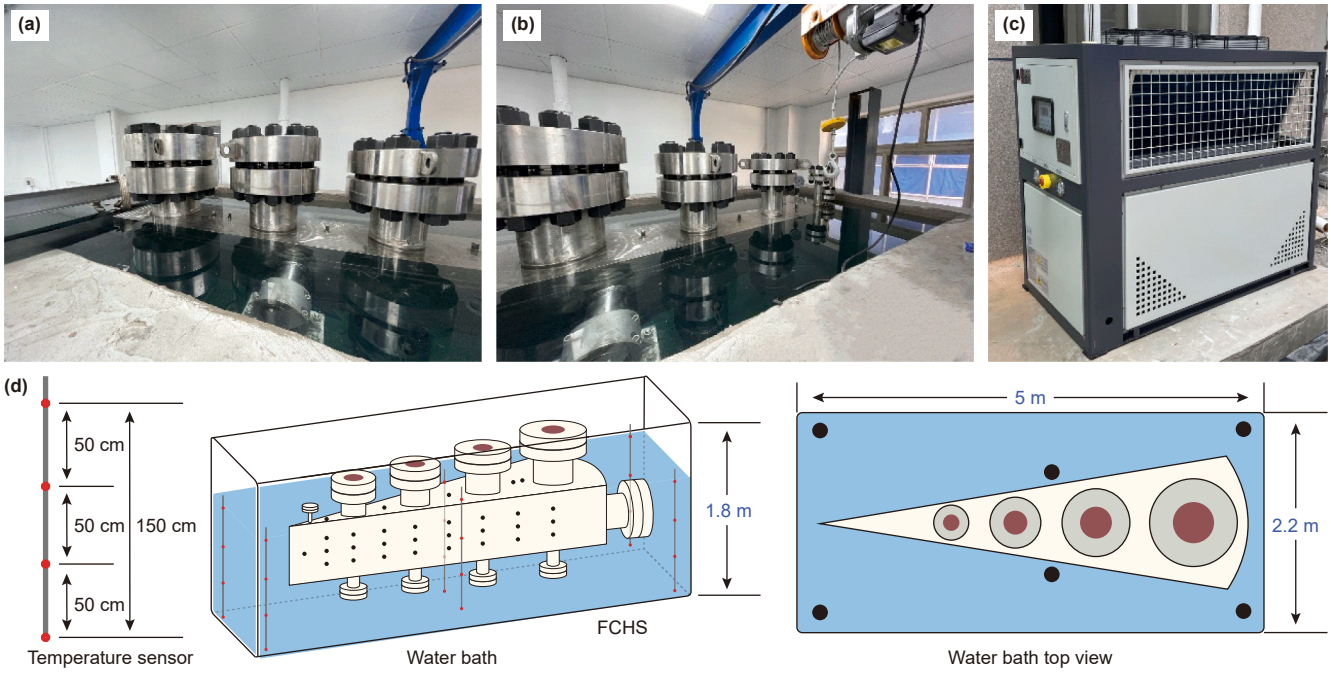

Fig. 8. Temperature control system: **(a–b)** actual picture of the FCHS within the water tank from various angles, **(c)** actual picture of the refrigeration machine and **(d)** schematic diagram of the arrangement of 24 temperature measurement points.

4. Experimental materials and procedures

4.1. Experimental materials

Methane (purity: 99.9%) was supplied by Beijing Haipu Gas Industry Corporation. A brine solution (salinity: 3.35%) was prepared using NaCl sourced from Aladdin Industrial Corporation. Particle analysis of the quartz sand revealed a median particle size of 80.025 μm ($\phi_{50} = 79.62$ μm), which corresponds to a mesh size of ~200, as shown in Fig. 9. The mean true density of the quartz sand was measured at 3.4416 g/cm^3, with an estimated porosity of ~30.39%. All quartz sand was washed with deionized water and thoroughly dried prior to experiments.

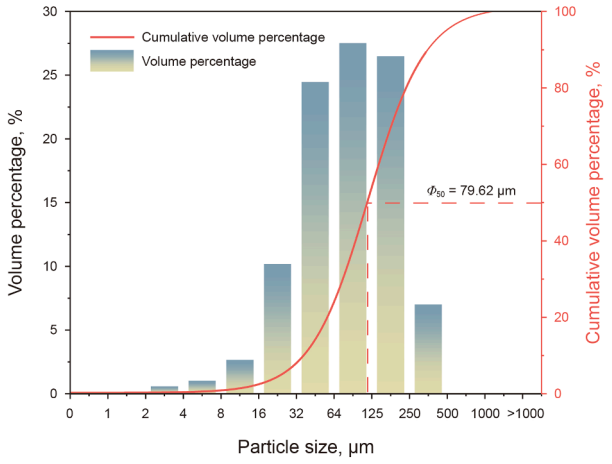

Fig. 9. Particle size distribution of the quartz sand.

4.2. Sand-packing

The FCHS is essentially a large-volume blind reactor, presenting challenges for complete filling with sand. This study introduces a novel method termed "water flow migration" to address the issue. The sand-packing procedure, illustrated in Fig. 10, involves the following steps:

Leveling and settling: The vessel was leveled once more and left to stand for ~12 h to flatten the mixture slope. This step, along with the previous one, was repeated 3–4 times until ~328.88 kg of dry

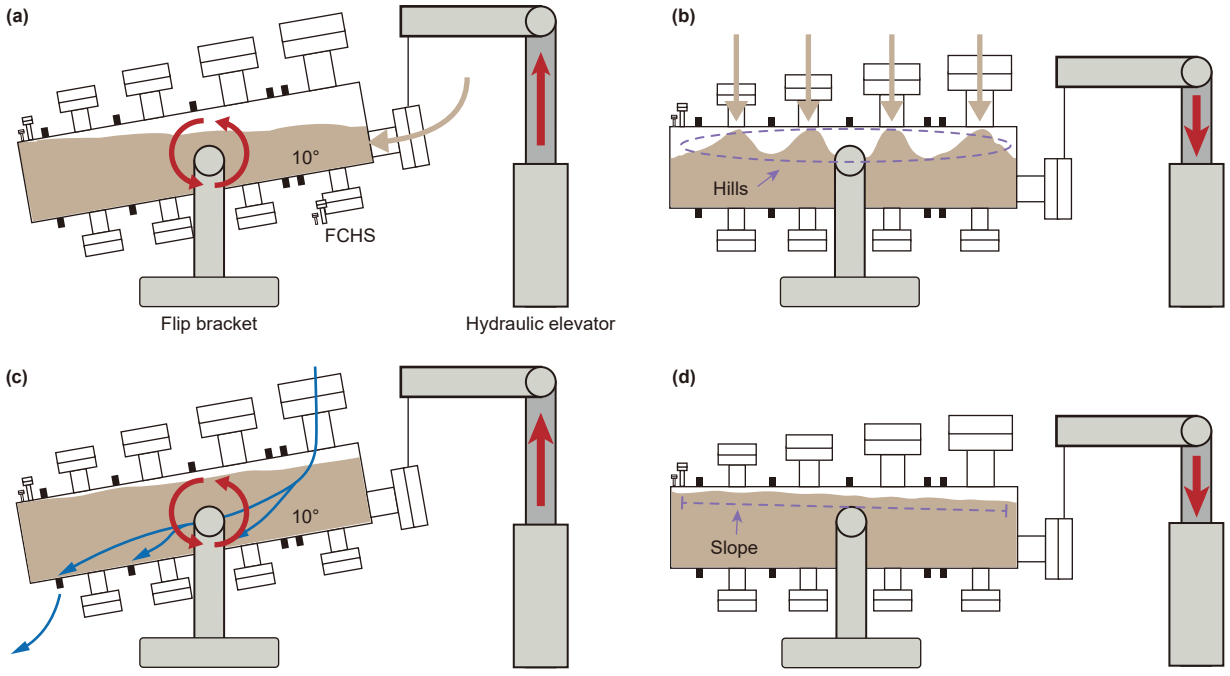

Fig. 10. Schematic diagram of the procedure for sand-packing within the FCHS.

sand achieved >95% filling, leaving ~1 cm of clearance between the mixture and the upper wall.

As shown in Fig. 9, the grain size distribution facilitated the settling of finer particles in the lower layers, thereby resulting in higher compactness and reduced permeability. The sediments exhibited an average porosity of ~30.39%, closely mimicking natural deposits (Liu et al., 2022). This novel method effectively minimizes blind zones in the FCHS, obtaining sediment samples that are representative of natural conditions. The V_P data measured at various radial positions were consistently ~850 m/s, suggesting that the pore structure of the sediments exhibited good radial homogeneity.

4.3. Application of phase change material

After sand-packing, less than 5% of the cavity remained unfilled, which significantly impacted experimental results. As shown in Fig. 11, the residual unfilled space reduces fluid flow resistance compared to the lower sediment layers, resulting in the "wall effect". Specifically, this effect denotes the influence of physical boundaries (e.g., the simulator wall) on fluid flow within the sediments. Such interference can lead to abnormal fluid flow, thereby undermining the reliability of experimental data.

To eliminate the "wall effect", phase change material (PCM) with a fixed transition temperature (T_{tra}) was introduced to occupy the residual unfilled space. In its liquid state, the PCM exhibits low viscosity, which facilitates pipeline transport and ensures complete filling of the target space.

The chosen PCM, a commercially available liquid alkane mixture from Shanghai Lingbo Technology, exhibits approximately 15% volume shrinkage upon solidification, as depicted in Fig. 12. A T_{tra} of 17 °C was selected due to the lack of heating capabilities in water bath and typical winter laboratory temperatures not exceeding 15 °C. The utilization process is illustrated in Fig. 13 and involves the following steps:

Preparation: After sand-packing, the simulated sediments were saturated with brine, and the vessel was then evacuated for liquid PCM injection.

Injection: Liquid PCM was injected into the vessel via pipelines until the system pressure reached 0.5 MPa, ensuring complete filling of the unoccupied space.

Compensation for shrinkage: To effectively counteract volume shrinkage during solidification, additional liquid PCM was injected to prevent the formation of new voids upon cooling. The penetration depth of PCM into the sediments was calculated based on the displaced water volume and sediment porosity, typically achieving an immersion depth of ~1 cm.

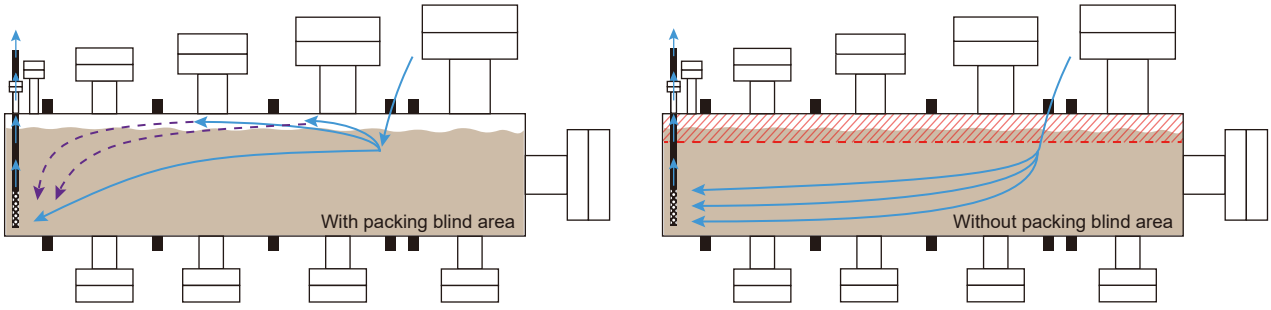

Fig. 11. Comparison of the usage effects of liquid-solid PCM.

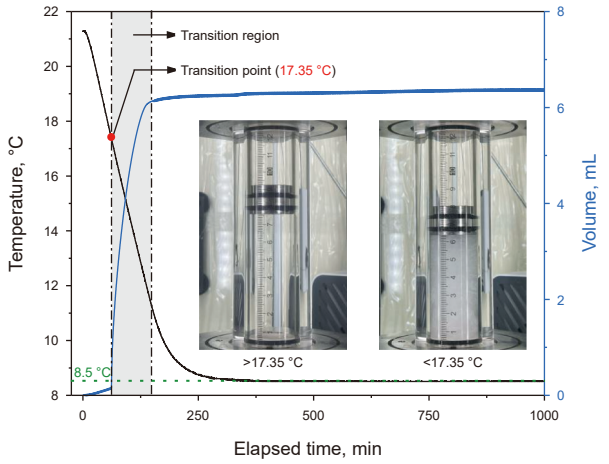

Fig. 12. Volume changes of the liquid-solid PCM during the phase transition under constant pressure conditions (7 MPa).

Solidification: Under constant pressure, the temperature of the vessel was gradually reduced to solidify the injected liquid PCM. Notably, owing to the intrinsic insolubility of liquid alkanes in brine, both the liquid and solidified states of the PCM remain insoluble. Therefore, the influence of PCM on the pore brine can be negligible.

To validate the effectiveness of PCM in eliminating the "wall effect", comparative experiments were conducted. Brine replenishment at the vessel's broad-end simulated fluid generation from hydrate dissociation, with the injection rate controlled via DMP power. The experimental conditions are summarized in Table 1, and the results are shown in Fig. 14.

Fig. 14 demonstrates that in scenarios including PCM (Runs 1–3), a direct correlation exists between the pressure difference and the brine injection rate. With the production well connected to the atmosphere, the pressure difference primarily reflects conditions near the vessel's broad-end. An increased brine injection rate resulted in a higher pressure difference due to flow resistance within the sediments, thereby confirming the effectiveness of PCM in eliminating the "wall effect". In contrast, scenarios excluding PCM (Runs 4–6) exhibited negligible pressure differences, as fluids preferentially migrated through upper unfilled spaces with lower resistance, bypassing the sediments—a phenomenon known as

Table 1
The experimental conditions during brine replenishment.

Run	PCM	Location	Rate, mL/min
1	Including	Broad-end	50
2	Including	Broad-end	150
3	Including	Broad-end	200
4	Excluding	Broad-end	50
5	Excluding	Broad-end	150
6	Excluding	Broad-end	200

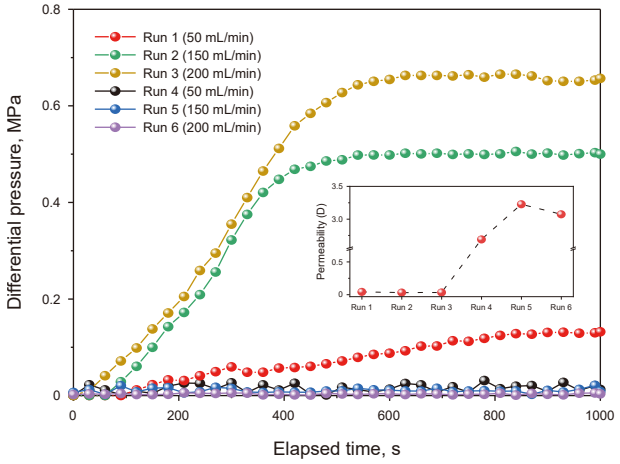

Fig. 14. The influence of PCM on the pressure difference. Runs 1–3 correspond to scenarios including PCM, while Runs 4–6 correspond to scenarios excluding PCM.

"fluid migration with short-circuit". Furthermore, the sediment permeability under various conditions has been calculated and is presented in the inset of Fig. 14. The detailed equations and calculation process for determining the sediment permeability (K_{sed}) are provided in Section 3 in the Supporting Information. It can be seen that the K_{sed} of runs including PCM are significantly lower than that of runs excluding PCM. Generally, a lower permeability indicates a higher resistance to fluid flow. Therefore, it can be concluded that PCM effectively eliminates the "wall effect" and improves data reliability.

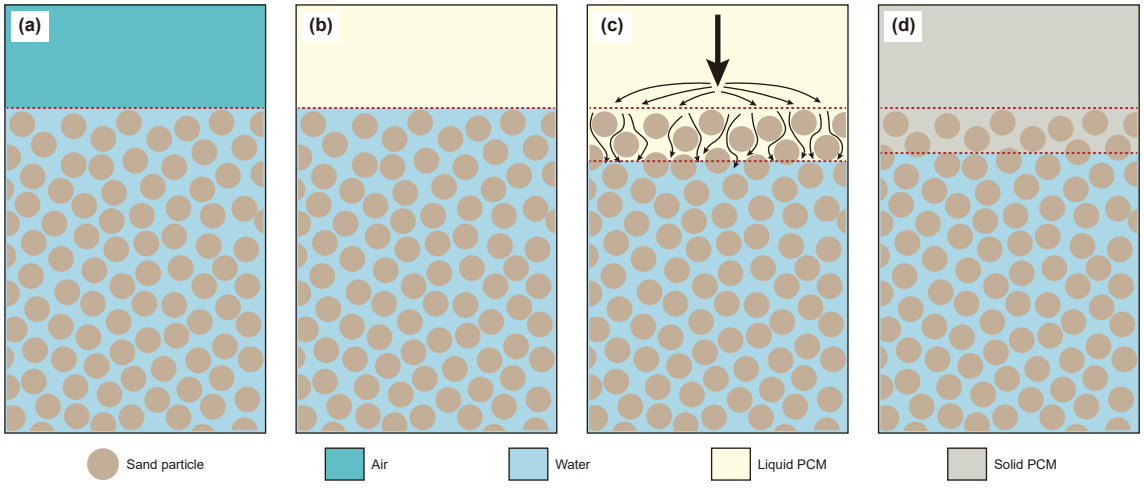

Fig. 13. Schematic diagram of the filling space with liquid-solid PCM.

4.4. Hydrate formation

To simulate realistic conditions, an aqueous-rich HBS sample was synthesized using a combination of excess-gas and excess-water methods. Following sand-packing and PCM injection, brine was injected from the vessel's bottom to 15 MPa for leakage testing. Once sealed, the vessel was depressurized to atmospheric pressure, and methane gas was injected to displace the pore brine for hydrate formation. To minimize heterogeneity in initial aqueous saturation (S_A), a "zonal gas flooding" strategy was employed. Specifically, the sediments were radially divided into multiple zones using symmetrically placed operation ports on the top and bottom of the reactor. For each zone, the required drainage volume was calculated based on the known sediment volume, porosity, and the target initial S_A. Methane gas was injected bottom-up within each zone to displace pore brine, with the zones processed sequentially from the narrow-end to the broad-end. The bottom-up gas flooding helped suppress the gravitational reaccumulation of brine in lower sediment layers. Once drainage in one zone was complete, the process proceeded to the adjacent zone. This stepwise "zonal gas flooding" strategy facilitated a more uniform distribution of initial S_A prior to hydrate formation. At last, set the water bath at 5 °C to accelerate the process of hydrate formation.

The average pressure (P_{avg}) and average temperature (T_{avg}) for various measurement points can be estimated as

$$P_{avg} = \frac{\sum_{i=1}^{4} UP_i + \sum_{i=1}^{9} MP_i + \sum_{i=1}^{4} LP_i}{17} \quad (1)$$

$$T_{avg} = \frac{\sum_{i=1}^{21} UT_i + \sum_{i=1}^{21} LT_i}{42} \quad (2)$$

where UP_i, MP_i, and LP_i represent the values of pressure transducers on various planes in Fig. 5, respectively; UT_i and LT_i represent the values of temperature sensors on various planes in Fig. 6, respectively.

Fig. 15 shows the typical evolution of average pressure (P_{avg}), average temperature (T_{avg}), and ambient temperature (T_{amb}) during synthesis. To achieve realistic S_H (hydrate saturation), multi-gas injections are performed at pressures of 10, 10, and 8.5 MPa (A–D), all exceeding the phase equilibrium pressure of hydrates (5 °C, 5.28 MPa) (Chen and Guo, 1998). After stabilizing P_{avg}, several rounds of pre-cooled brine injection consumed residual methane and created an aqueous-rich environment (D–G). Detailed information on the multiple injection process is listed in Table S1 in the Supporting Information. The minimal T_{avg} increase during the final brine injection indicated near-complete methane depletion.

Considering a typical seafloor temperature of 3 °C and a geothermal gradient of 20 °C/km, the water bath was gradually increased from 5 to 8.5 °C to mimic geological conditions in the China Shenhu Area (201–298 mbsf (Li et al., 2018a)) (G–H). Hydrate formation was deemed complete when the pressure drop fell below 0.005 MPa/h. The final V_P values, ranging between 1800 and 1900 m/s across radial positions, indicate a reasonably good macroscopic homogeneity in hydrate saturation (S_H). Final phase saturations were calculated based on previous studies (Wang et al., 2020; Yuan et al., 2013), yielding S_H of 42.96%, S_A of 55.11%, and S_G of 1.93%. The detailed calculation procedures for each phase saturation are provided in Section 3 in the Supporting Information. Generally, NGH reservoirs with S_H greater than 40% align with geological surveys (Boswell et al., 2019), and are favorable for long-term, economically viable production, as indicated by reservoir assessments (Moridis et al., 2011). Thus, the synthesized aqueous-rich HBS sample provides a robust foundation for simulating field tests (Wang et al., 2018; Zhao et al., 2014).

4.5. Hydrate exploitation test

Depressurization is the most promising exploitation method, favored for its simplicity, ease of operation, and low costs (Oyama et al., 2012; Shi et al., 2021). In this work, production behaviors were simulated using the newly developed hydrate simulator. Upon hydrate formation, gas collectors and a gas-liquid separator were evacuated at least 30 min in preparation for the exploitation test. A DMP was connected to the vessel's broad-end to inject high-pressure, pre-cooled brine, simulating seepage phenomena in an unsealed system. P_{prod} was set at 3 MPa by adjusting the BPV, and experiments commenced with the globe valve (V16) opening. Fig. 16 illustrates the temporal evolution of the key parameters. A concise overview of the production process is given in this section, with in-depth analysis deferred to Section 5.1. During the depressurization (DP) stage, P_{avg} gradually decreased to P_{prod}, while the opening degree of the PCV was gradually increased to achieve a moderate depressurization rate. Hydrate dissociation continued at P_{prod} during the constant-pressure (CP) stage. The

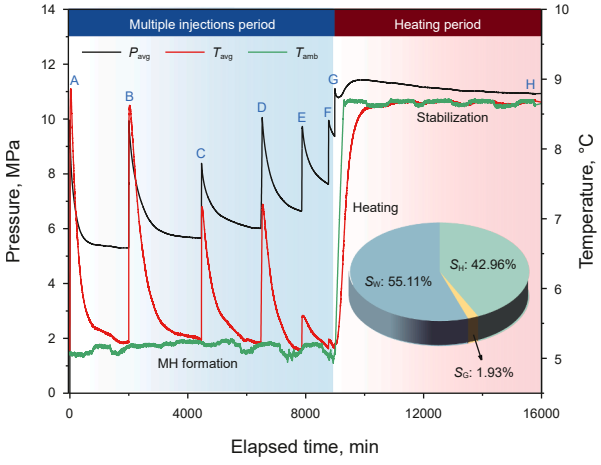

Fig. 15. Evolutions of P_{avg}, T_{avg} and T_{amb} over time during the synthesis of aqueous-rich HBS sample (A–H refers to the end of each stage). The final saturation of various phases is shown in the inset.

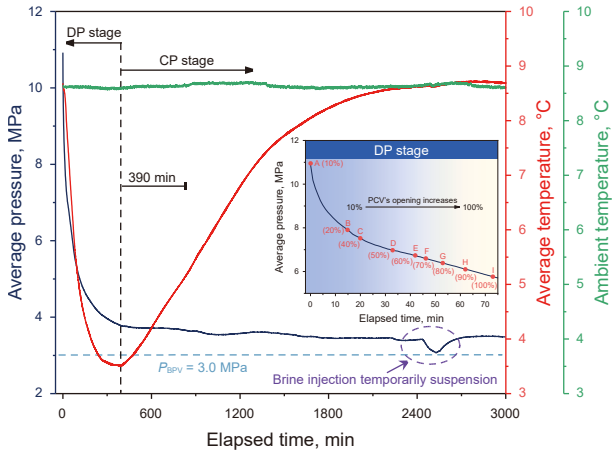

Fig. 16. Evolutions of average pressure, average temperature and ambient temperature. The inset shows the variation of PCV's orifice size over time.

fluids dissociated from hydrates flowed into the gas-liquid separator, where brine was retained, and methane gas was collected in a gas collector. The separated brine was periodically discharged and quantified. When the pressure in the gas collector approached 3 MPa, a standby gas collector was employed to ensure continuous gas collection. At last, T_{avg} was increased to T_{amb}, and data recording ceased.

The gas production rate ($r_{prod(G),t}$) is calculated as the molar amount of gas production per minute.

$$r_{prod(G),t} = n_{prod(G),t+1} - n_{prod(G),t} \tag{3}$$

where $n_{prod(G),t+1}$ and $n_{prod(G),t}$ represent the mole amount for methane production at specified time of t+1 and t, respectively.

Similarly, the rates of brine injection ($r_{inj(W),t}$) and production ($r_{prod(W),t}$) are calculated as:

$$r_{inj(W),t} = V_{inj(W),t+1} - V_{inj(W),t} \tag{4}$$

$$r_{prod(W),t} = V_{prod(W),t+1} - V_{prod(W),t} \tag{5}$$

where $V_{inj(W),t+1}$ and $V_{inj(W),t}$ represent the volume amount for brine injection at specified time of t+1 and t, respectively; $V_{prod(W),t+1}$ and $V_{prod(W),t}$ represent the volume amount for brine production at specified time t +1 and t, respectively.

Water to gas ratio ($R_{WG,t}$) is a key parameter in the evaluation of fluid production potential from reservoirs, can be estimated as:

$$R_{WG,t} = n_{prod(W),t} \Big/ n_{prod(G),t} \tag{6}$$

where $n_{prod(W),t}$ represents the mole amount for brine production at specified time of t.

5. Simulation results and discussion

To evaluate the overall functionality of the experimental system centered on the FCHS, a depressurization-induced production experiment was conducted using an unsealed HBS sample. Significant data were collected in detail, and the primary results are presented below.

5.1. Production behaviors

Fig. 16 shows the temporal evolutions of P_{avg}, T_{avg}, and T_{amb}, with the inset depicting the dynamic adjustment of the PCV to mimic the field operation procedure. Upon starting the experiment, P_{avg} gradually declines before stabilizing at around 4 MPa. The experiment is categorized into the DP and CP stages at ~390 min, following a classic division method. Notably, P_{avg} does not reach P_{prod} due to external brine infiltration, a phenomenon often mentioned in literatures concerning unsealed marine reservoir exploitation (Cui et al., 2024; Sun et al., 2019, 2022). Overall, the time-dependent variation of T_{avg} displays a typical V-shaped trend, which objectively reflects the thermal response of the reservoir during hydrate dissociation. T_{amb} exhibits fluctuations within ±0.2 °C, indicating effective temperature control throughout the long-term experimental process.

Fig. 17 shows the performances of brine injection and production. The abundant availability of pore brine causes a Gaussian-like curve change in $R_{prod(W),t}$. Its value experiences a rapid increase to a peak shortly after the experiment begins, followed by a gradual decline until stabilizing at around 30 mL/min. On the other hand, a significant increase in $R_{inj(W),t}$ occurs during the DP stage, which correlates with the accelerated seepage of external brine as reservoir pressure decreases (Zhao et al., 2020). Upon reaching the

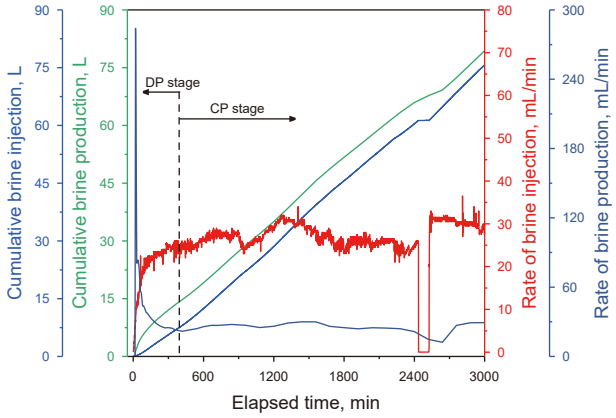

Fig. 17. Brine injection and production performances.

CP stage, the upward trend of $R_{inj(W),t}$ flattens and stabilizes at a value close to that of $R_{prod(W),t}$, suggesting a dynamic equilibrium in brine flow. The difference between $V_{prod(W),t}$ and $V_{inj(W),t}$ represents the net brine production, mainly from hydrate dissociation.

Fig. 18 shows gas production performance, accompanied by an inset plotting the temporal evolution of $R_{WG,t}$. The curve trajectory of $R_{prod(G),t}$ mirrors that of $R_{prod(W),t}$, primarily due to the correlation between fluid production and hydrate dissociation. However, the peak of $R_{prod(G),t}$ lags behind that of $R_{prod(W),t}$, indicating that the relatively lower effective permeability of gas in aqueous-rich reservoirs delays gas production (Li et al., 2024; Zhao et al., 2016). During the CP stage, $R_{WG,t}$ exhibits continuous increase, which aligns with a numerical simulation conducted over a time scale of 2000 days (Oluwunmi et al., 2023). Furthermore, brine invasion exacerbates as exploitation progresses, highlighting the need for reservoir reformation technology.

Fig. 19 shows the ultrasonic response of the reservoir during the experiment. Initially, the consolidation effect of hydrates results in higher V_P values (Li et al., 2011). As hydrate dissociation progresses, V_P exhibits an overall downward trend, with the observed order being $V_{P4} > V_{P3} > V_{P2} > V_{P1}$. Given the positive correlation between V_P and S_H (Waite et al., 2004; Winters et al., 2004), as well as the role of hydrates in maintaining reservoir stability (Waite et al., 2009; Zhu et al., 2024), the variations in V_{P1-4} not only

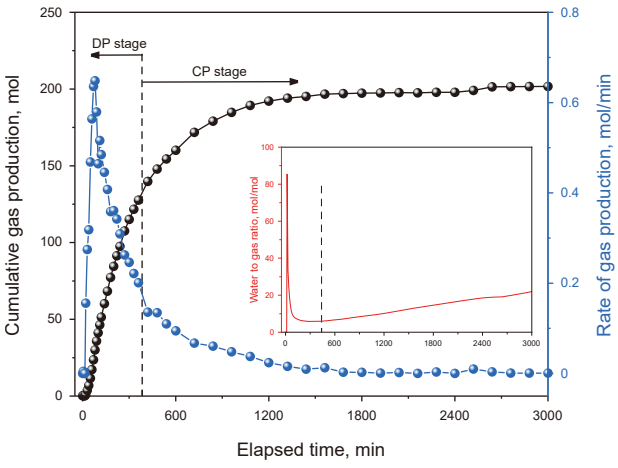

Fig. 18. Gas production performance. The inset shows the evolution of water to gas ratio over time.

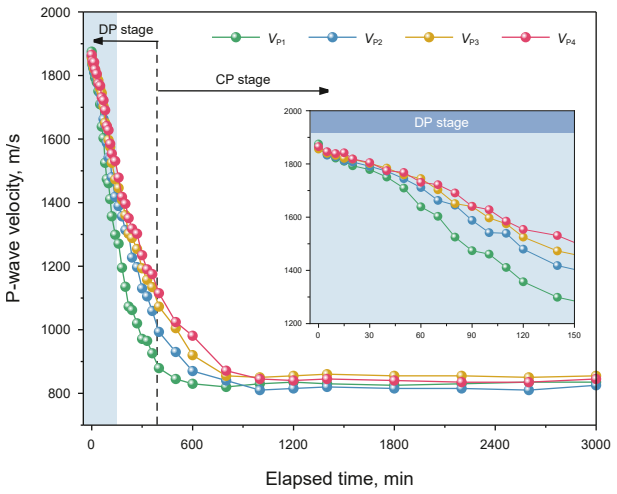

Fig. 19. Variations of P-wave velocities over time. The initial 150 min is shown in the inset.

reflect the loss of stratum stiffness along the radial direction within the reservoir but also provide insights into the movement of the dissociation front.

In general, the functions of each subsystem have been tested through the simulated experiment. The observed production behaviors conform to the typical characteristics of hydrate dissociation and are also appeared in other large-volume simulators (Huang et al., 2023; Konno et al., 2014; Li et al., 2012c), indicating the reliability of the data. Furthermore, the comparability results with offshore field tests, such as those conducted in the Nankai Trough of Japan (Konno et al., 2017; Yamamoto et al., 2014, 2019) and the Shenhu Area of China (Li et al., 2018a; Ye et al., 2020), presents the rationality of using brine replenishment to simulate seepage phenomena, which will significantly enhance the authenticity of the data. Consequently, the FCHS, equipped with comprehensive control and monitoring features, has proven to be an exceptional platform for studying the complex production behaviors of NGH reservoirs under laboratory conditions.

5.2. Pressure field

Fig. 20 shows the spatio-temporal evolution of the pressure field, wherein two distinct color scales were used to correspond to DP and CP stages, thereby enhancing recognition. In this section, based on the principle of symmetry, the fan-shaped plane within the FCHS was equivalently expanded to the entire circular range to fit with natural reservoirs. Similar methodologies have also been applied in the subsequent presentation of temperature and hydrate saturation fields. To facilitate a better understanding of the "equivalent extension principle" used for multi-field spatio-temporal evolution, a schematic diagram is provided in Fig. S1 in the Supporting Information. As fluid production occurs, a lower-pressure zone emerges near the production well and continues to expand. Meanwhile, the pressure gradient gradually decreases from an initial value of ~9 MPa, ultimately stabilizing at ~0.3 MPa. This trend objectively reflects the changes in reservoir permeability induced by hydrate dissociation (Li et al., 2022) and the adverse effects of seepage phenomena on radial pressure propagation (Gu et al., 2023; Sun et al., 2023). Overall, the FCHS has successfully constructed a spatio-temporal evolution pattern of the pressure field that is comparable to trial productions in the Nankai Trough of Japan (Konno et al., 2017; Yamamoto et al., 2019), verifying the authenticity and accuracy of the obtained data. The acquisition of pressure gradient provides key insights into fluid flow behavior and pressure propagation efficiency within HBS. It serves as a fundamental parameter for evaluating reservoir permeability, identifying preferential seepage pathways, and characterizing the spatial heterogeneity induced by hydrate dissociation. Moreover, detailed pressure gradient analysis allows for better control of depressurization strategies, aiding in the prevention of rapid pressure drops that may trigger hydrate reformation or geomechanical instability. Unlike traditional cylinder-shaped simulators, which exhibit a uniform pressure distribution under limited simulation scales, this novel simulator more effectively captures dynamic changes within reservoirs, thus providing a more reliable experimental basis for parameter optimization, production prediction, and behavior analysis in field tests (Ge et al., 2023; Heeschen et al., 2016; Huang et al., 2023; Konno et al., 2014; Li et al., 2012a; Wang et al., 2020).

5.3. Temperature field

Fig. 21 shows the spatio-temporal evolution of the temperature field. Upon production initiation, the expansion of the low-temperature range, caused by the cooling effect from local hydrate dissociation, closely aligns with the previously mentioned low-pressure region. Subsequently, as the dissociation intensity attenuates within the near-well region, the reservoir center takes the lead in increasing temperature. These observed phenomena have been verified by numerous numerical simulations and field tests (Dong et al., 2022; Feng et al., 2019; Huang et al., 2015; Moridis et al., 2013; Qin et al., 2020; Sun et al., 2015, 2017). However, traditional cylinder-shaped simulators generally exhibit a warming trend from the boundary towards the center during the temperature recovery process, mainly due to excessive radial heat transfer. Take the Shenhu Area of the South China Sea as an example; the HBS covers an area of 6.42 km^2 with a mean thickness of 57 m (Li et al., 2018a). Hereinto, the relatively small aspect ratio means that vertical transfer from the overlying and underlying strata dominates the reservoir thermal response, which is well reflected within the FCHS. Overall, accurately capturing the evolution of the temperature field is crucial for optimizing thermal management strategies and improving production efficiency in field-scale hydrate exploitation. A precise understanding of the thermal regime provides a solid foundation for predicting heat transfer behavior, hydrate dissociation kinetics, and reservoir stability. This highlights the importance of employing well-configured experimental simulators to ensure the reliability and representativeness of simulation results, particularly under complex and large-scale heat transfer conditions characteristic of actual hydrate production scenarios.

5.4. Hydrate saturation field

Given the positive correlation between V_P and S_H (Ren et al., 2010), a rough inversion of S_H was performed based on the decreases in V_{P1-4}, and the resulting spatial-temporal evolution of the hydrate saturation field is shown in Fig. 22. It can be seen that there is a decreasing trend of S_H spreading from the production well within the reservoir, indicating the movement of the hydrate dissociation front. Furthermore, the initial rapid increase in the advancing speed of the hydrate dissociation front, followed by a gradual deceleration, is consistent with the typical evolution pattern of hydrate dissociation intensity (Li et al., 2014). On the whole, the radial evolution of S_H correlates well with the production behaviors triggered by low pressure in the wellbore, as reported in numerous studies (Lu et al., 2022; Moon et al., 2023; Su et al., 2012b; Xiao et al., 2022). In contrast to other large-volume

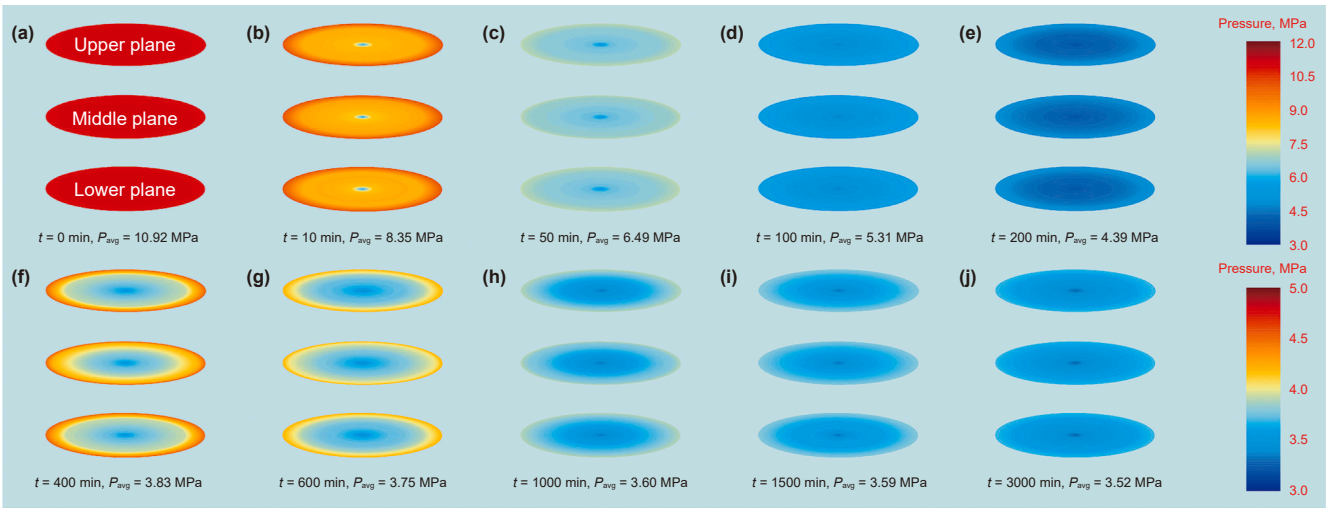

Fig. 20. Spatio-temporal evolution of the pressure field.

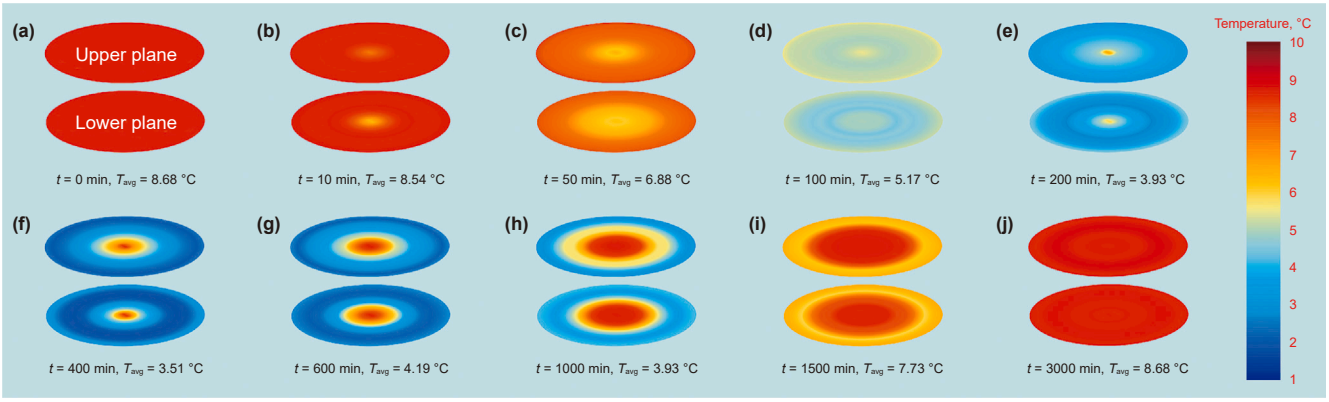

Fig. 21. Spatio-temporal evolution of the temperature field.

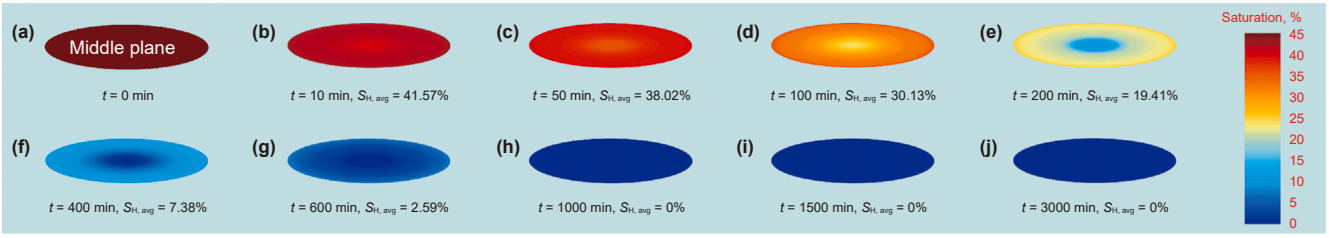

Fig. 22. Spatio-temporal evolution of the hydrate saturation field.

simulators that primarily rely on conventional pressure and temperature data monitoring, the hydrate saturation field has been well-established within the FCHS through the integration of in-situ acoustic detection technology, thus further improving the comprehensiveness of the multi-field evolution obtained. At present, the inversion of S_H based on V_P remains relatively simple, allowing only a preliminary understanding of S_H evolution trends rather than providing accurate quantitative analyses. Future research should focus on improving the V_P-S_H models and developing more reliable predictive frameworks to capture the spatio-temporal evolution of S_H field with greater precision. Moreover, the current detection techniques remain relatively limited in scope; thus, integrating additional sensors capable of measuring S_G and S_A could significantly improve the predictive capability of the concentration field evolution and further enhance the overall understanding of multiphase flow dynamics within HBS.

From a practical application perspective, the main purpose of constructing large volume simulators is to obtain spatio-temporal evolution of multi-field for resource exploitation guidance. However, achieving this remains challenging due to the limitations of radial simulation scales. With the implementation of a novel shape design, the FCHS effectively address the existing conundrum, and the reliability of the constructed multi-field structure has been validated. Compared to cylinder-shaped simulators, the FCHS exhibits several distinct advantages. A diagram is provided to visually highlight the advantages (see Table 2). In this work, the pressure

Table 2
Comparation between several large-volume simulators[a].

Parameter	PHS	FCHS	TDHS	LARS	FLYS	HIGUMA	LHRS
Effect volume, L	117.8	142	196	210	282.6	810	1600
Equivalent volume, L	117.8	8520	196	210	282.6	810	1600
Detection method	P, T, R	P, T, A	P, T, R	P, T, R	P, T	P, T	P, T
Pressure gradient, m	–	3	–	–	–	–	–
Field evolution	T, R	P, T, A	T, R	T, R	T	T	T

[a] The letters P, T, R, and A represent pressure, temperature, resistance, and acoustic, respectively.

field was established for the first time, correcting a long-standing error in the evolution of temperature field, and greatly enriching multi-field research via the application of acoustic detection technology. The multi-field evolution obtained from FCHS experiments, including acoustic-based hydrate saturation field, pressure propagation patterns, and thermal front evolution, provide valuable benchmark datasets for numerical model validation.

6. Conclusions

The development of the FCHS has successfully addressed the challenges of manufacturing full-dimensional, large-scale high-pressure vessels, and has improved the timeliness and safety of their usage. This novel apparatus aims to investigate the formation and evolution of multi-field spatio-temporal structures and regulatory methods, thereby contributing to the environmentally sustainable and efficient utilization of NGH resources. Rigorous experimental tests have validated the multifunctionality of the entire simulation system, demonstrating the feasibility of mimicking the representative nature NGH reservoirs. Meanwhile, the production behaviors observed during the experiment, such as hydrate dissociation, fluid flow, and wave propagation, prove the effectiveness of each subsystem.

Based on the innovative structural design, the representative temperature and pressure fields during the hydrate exploitation process have been successfully established within the FCHS. The application of ultrasonic probes also provides effective assistance in in-situ monitoring the hydrate dissociation within sediments. Therefore, this large-scale fan column-shaped apparatus is a remarkable experimental system in terms of flexibility and versatility for simulating the hydrate formation process, hydrate production process, and marine hydrate-based CO_2 sequestration process. The FCHS will provide an important large-scale simulation scenario for optimizing the hydrate exploitation process, developing new and efficient techniques, and evaluating the effectiveness of reservoir modification and other production enhancement methods.

CRediT authorship contribution statement

Ling-Ban Wang: Writing – original draft, Methodology, Investigation. **Xiao-Hui Wang:** Methodology. **Yu-Hao Bu:** Investigation. **Zhen-Bin Xu:** Investigation. **Xian Sun:** Investigation. **Yi-Fei Sun:** Formal analysis. **Peng Xiao:** Data curation. **Qing-Ping Li:** Funding acquisition. **Shou-Wei Zhou:** Validation. **Praveen Linga:** Writing – review & editing, Validation. **Chang-Yu Sun:** Writing – review & editing, Supervision, Conceptualization. **Guang-Jin Chen:** Writing – review & editing, Methodology, Conceptualization.

Declaration of competing interest

The authors declare that they have no known competing financial interests or personal relationships that could have appeared to influence the work reported in this paper.

Acknowledgements

Financial support received from the National Natural Science Foundation of China (22127812, 22578482, 22278433), the National Key Research and Development Program of China (2021YFC2800902) is gratefully acknowledged.

Appendix A. Supplementary data

Supplementary data to this article can be found online at https://doi.org/10.1016/j.petsci.2025.10.003.

References

Boswell, R., Collett, T.S., 2011. Current perspectives on gas hydrate resources. Energy Environ. Sci. 4 (4), 1206–1215. https://doi.org/10.1039/c0ee00203h.
Boswell, R., Myshakin, E., Moridis, G., et al., 2019. India National Gas Hydrate Program Expedition 02 summary of scientific results: numerical simulation of reservoir response to depressurization. Mar. Petrol. Geol. 108, 154–166. https://doi.org/10.1016/j.marpetgeo.2018.09.026.
Chen, G., Guo, T., 1998. A new approach to gas hydrate modelling. Chem. Eng. J. 71 (2), 145–151. https://doi.org/10.1016/S1385-8947(98)00126-0.
Cui, J., Wang, X., Li, Y., et al., 2024. Influence of gravity on methane hydrate dissociation characteristics by depressurization in marine hydrate reservoirs. Energy 296, 131133. https://doi.org/10.1016/j.energy.2024.131133.
Demirbas, A., 2010. Methane hydrates as potential energy resource: part 1–Importance, resource and recovery facilities. Energy Convers. Manag. 51 (7), 1547–1561. https://doi.org/10.1016/j.enconman.2010.02.013.
Dong, B., Xiao, P., Sun, Y., et al., 2022. Coupled flow and geomechanical analysis for gas production from marine heterogeneous hydrate-bearing sediments. Energy 255, 124501. https://doi.org/10.1016/j.energy.2022.124501.
Feng, J., Li, B., Li, X., et al., 2021. Effects of depressurizing rate on methane hydrate dissociation within large-scale experimental simulator. Appl. Energy 304, 117750. https://doi.org/10.1016/j.apenergy.2021.117750.
Feng, Y., Chen, L., Suzuki, A., et al., 2019. Numerical analysis of gas production from layered methane hydrate reservoirs by depressurization. Energy 166, 1106–1119. https://doi.org/10.1016/j.energy.2018.10.184.
Ge, Y., Li, Q., Lv, X., et al., 2023. A large-scale experimental simulator for natural gas hydrate recovery and its experimental applications. Petroleum 9 (4), 607–612. https://doi.org/10.1016/j.petlm.2021.12.005.
Gu, Y., Sun, J., Qin, F., et al., 2023. Enhancing gas recovery from natural gas hydrate reservoirs in the eastern Nankai Trough: deep depressurization and underburden sealing. Energy 262, 125510. https://doi.org/10.1016/j.energy.2022.125510.
Heeschen, K.U., Abendroth, S., Priegnitz, M., et al., 2016. Gas production from methane hydrate: a laboratory simulation of the multistage depressurization test in Mallik, Northwest Territories, Canada. Energy Fuel 30 (8), 6210–6219. https://doi.org/10.1021/acs.energyfuels.6b00297.
Huang, L., Kang, J., Bu, Q., et al., 2023. Experimental investigation of hydrate production via deep depressurization using a large-scale laboratory reactor. Energy Fuel 37 (4), 2799–2810. https://doi.org/10.1021/acs.energyfuels.2c03945.
Huang, L., Su, Z., Wu, N., 2015. Evaluation on the gas production potential of different lithological hydrate accumulations in marine environment. Energy 91, 782–798. https://doi.org/10.1016/j.energy.2015.08.092.
Konno, Y., Fujii, T., Sato, A., et al., 2017. Key findings of the World's first offshore methane hydrate production Test off the Coast of Japan: toward future commercial production. Energy Fuel 31 (3), 2607–2616. https://doi.org/10.1021/acs.energyfuels.6b03143.
Konno, Y., Jin, Y., Shinjou, K., et al., 2014. Experimental evaluation of the gas recovery factor of methane hydrate in sandy sediment. RSC Adv. 4 (93), 51666–51675. https://doi.org/10.1039/c4ra08822k.
Li, B., Li, X., Li, G., et al., 2014. Depressurization induced gas production from hydrate deposits with low gas saturation in a pilot-scale hydrate simulator. Appl. Energy 129, 274–286. https://doi.org/10.1016/j.apenergy.2014.05.018.
Li, F., Sun, C., Zhang, Q., et al., 2011. Laboratory measurements of the effects of Methane/Tetrahydrofuran concentration and grain size on the P-wave velocity

of hydrate-bearing sand. Energy Fuel. 25 (5), 2076–2082. https://doi.org/10.1021/ef101665v.
Li, G., Li, B., Li, X., et al., 2012a. Experimental and numerical studies on gas production from methane hydrate in porous media by depressurization in pilot-scale hydrate simulator. Energy Fuel 26 (10), 6300–6310. https://doi.org/10.1021/ef301229k.
Li, J., Ye, J., Qin, X., et al., 2018a. The first offshore natural gas hydrate production test in South China Sea. Chin Geol. 1 (1), 5–16. https://doi.org/10.31035/cg2018003.
Li, M., Zhou, S., Wu, P., et al., 2022. Permeability analysis of hydrate-bearing sediments considering the effect of phase transition during the hydrate dissociation process. J. Nat. Gas Sci. Eng. 97, 104337. https://doi.org/10.1016/j.jngse.2021.104337.
Li, N., Sun, Z., Sun, C., et al., 2018b. Simulating natural hydrate formation and accumulation in sediments from dissolved methane using a large three-dimensional simulator. Fuel 216, 612–620. https://doi.org/10.1016/j.fuel.2017.11.112.
Li, N., Zhang, J., Xia, M., et al., 2021. Gas production from heterogeneous hydrate-bearing sediments by depressurization in a large-scale simulator. Energy 234, 121183. https://doi.org/10.1016/j.energy.2021.121183.
Li, X., Yang, B., Li, G., et al., 2012b. Experimental study on gas production from methane hydrate in porous media by huff and puff method in Pilot-Scale Hydrate Simulator. Fuel 94, 486–494. https://doi.org/10.1016/j.fuel.2011.11.011.
Li, X., Yang, B., Zhang, Y., et al., 2012c. Experimental investigation into gas production from methane hydrate in sediment by depressurization in a novel pilot-scale hydrate simulator. Appl. Energy 93, 722–732. https://doi.org/10.1016/j.apenergy.2012.01.009.
Li, Y., Wei, Z., Wang, H., et al., 2024. Impact of hydrate spatial heterogeneity on gas permeability in hydrate-bearing sediments. Energy 293, 130717. https://doi.org/10.1016/j.energy.2024.130717.
Liu, C., Li, Y., Liu, L., et al., 2020. An integrated experimental system for gas hydrate drilling and production and a preliminary experiment of the depressurization method. Nat. Gas. Ind. B. 7 (1), 56–63. https://doi.org/10.1016/j.ngib.2019.06.003.
Liu, C., Meng, Q., He, X., et al., 2015. Characterization of natural gas hydrate recovered from Pearl River Mouth basin in South China Sea. Mar. Petrol. Geol. 61, 14–21. https://doi.org/10.1016/j.marpetgeo.2014.11.006.
Liu, L., Wan, Y., Li, C., et al., 2022. Advances in field testing of the effective absolute permeability of gas hydrate reservoirs. Mar. Geol. Front. 38 (11), 40–55. https://doi.org/10.16028/j.1009-2722.2022.232.
Lu, C., Qin, X., Ma, C., et al., 2022. Investigation of the impact of threshold pressure gradient on gas production from hydrate deposits. Fuel 319, 123569. https://doi.org/10.1016/j.fuel.2022.123569.
Lu, H., Lorenson, T.D., Moudrakovski, I.L., et al., 2011. The characteristics of gas hydrates recovered from the Mount Elbert gas hydrate stratigraphic test well, Alaska North Slope. Mar. Petrol. Geol. 28 (2), 411–418. https://doi.org/10.1016/j.marpetgeo.2010.01.002.
Milkov, A.V., Sassen, R., 2002. Economic geology of offshore gas hydrate accumulations and provinces. Mar. Petrol. Geol. 19 (1), 1–11. https://doi.org/10.1016/S0264-8172(01)00047-2.
Moon, S.Y., Shin, H.J., Lim, J.S., 2023. Field-scale simulation of gas hydrate dissociation behavior in multilayered sediments under different depressurization conditions. J. Pet. Sci. Eng. 220, 111221. https://doi.org/10.1016/j.petrol.2022.111221.
Moridis, G.J., Kim, J., Reagan, M.T., et al., 2013. Feasibility of gas production from a gas hydrate accumulation at the UBGH2-6 site of the Ulleung basin in the Korean East Sea. J. Pet. Sci. Eng. 108, 180–210. https://doi.org/10.1016/j.petrol.2013.03.002.
Moridis, G.J.J., Collett, T.S.S., Pooladi-Darvish, M., et al., 2011. Challenges, uncertainties, and issues facing gas production from gas-hydrate deposits. SPE Reservoir Eval. Eng. 14 (1), 76–112. https://doi.org/10.2118/131792-pa.
Nagao, J., 2012. Development of methane hydrate production method—A large-scale laboratory reactor for methane hydrate production tests. Synthesiology 5 (2), 89–97. https://doi.org/10.5571/synth.5.89.
Oluwunmi, P.A., Reagan, M.T., Pecher, I.A., et al., 2023. Possible influx of seawater during gas production from unsealed gas hydrate reservoirs has economic and environmental implications. Energy Fuel 37 (23), 18843–18854. https://doi.org/10.1021/acs.energyfuels.3c02963.
Oyama, H., Konno, Y., Suzuki, K., et al., 2012. Depressurized dissociation of methane-hydrate-bearing natural cores with low permeability. Chem. Eng. Sci. 68 (1), 595–605. https://doi.org/10.1016/j.ces.2011.10.029.
Priegnitz, M., Thaler, J., Spangenberg, E., et al., 2013. A cylindrical electrical resistivity tomography array for three-dimensional monitoring of hydrate formation and dissociation. Rev. Sci. Instrum. 84 (10), 104502. https://doi.org/10.1063/1.4825372.
Qin, X., Liang, Q., Ye, J., et al., 2020. The response of temperature and pressure of hydrate reservoirs in the first gas hydrate production test in South China Sea. Appl. Energy 278, 115649. https://doi.org/10.1016/j.apenergy.2020.115649.
Ren, S., Liu, Y., Liu, Y., et al., 2010. Acoustic velocity and electrical resistance of hydrate bearing sediments. J. Pet. Sci. Eng. 70 (1), 52–56. https://doi.org/10.1016/j.petrol.2009.09.001.
Schicks, J., Spangenberg, E., Giese, R., et al., 2013. A counter-current heat-exchange reactor for the thermal stimulation of hydrate-bearing sediments. Energies 6 (6), 3002–3016. https://doi.org/10.3390/en6063002.
Schicks, J., Spangenberg, E., Giese, R., et al., 2011. New approaches for the production of hydrocarbons from hydrate bearing sediments. Energies 4 (1), 151–172. https://doi.org/10.3390/en4010151.
Shi, K., Wei, R., Guo, X., et al., 2021. Enhancing gas production from hydrate-bearing reservoirs through depressurization-based approaches: knowledge from laboratory experiments. Energy Fuel 35 (8), 6344–6358. https://doi.org/10.1021/acs.energyfuels.0c04075.
Su, K., Sun, C., Abhijit, D., et al., 2012a. Experimental investigation of hydrate accumulation distribution in gas seeping system using a large scale three-dimensional simulation device. Chem. Eng. Sci. 82, 246–259. https://doi.org/10.1016/j.ces.2012.07.029.
Su, Z., He, Y., Wu, N., et al., 2012b. Evaluation on gas production potential from laminar hydrate deposits in Shenhu Area of South China Sea through depressurization using vertical wells. J. Pet. Sci. Eng. 86–87, 87–98. https://doi.org/10.1016/j.petrol.2012.03.008.
Sun, J., Ning, F., Li, S., et al., 2015. Numerical simulation of gas production from hydrate-bearing sediments in the Shenhu area by depressurising: the effect of burden permeability. J. Unconv. Oil Gas Resour. 12, 23–33. https://doi.org/10.1016/j.juogr.2015.08.003.
Sun, J., Zhang, L., Ning, F., et al., 2017. Production potential and stability of hydrate-bearing sediments at the site GMGS3-W19 in the South China Sea: a preliminary feasibility study. Mar. Petrol. Geol. 86, 447–473. https://doi.org/10.1016/j.marpetgeo.2017.05.037.
Sun, Y., Cao, B., Chen, H., et al., 2023. Influences of pore fluid on gas production from hydrate-bearing reservoir by depressurization. Pet. Sci. 20 (2), 1238–1246. https://doi.org/10.1016/j.petsci.2022.09.015.
Sun, Y., Cao, B., Zhong, J., et al., 2022. Gas production from unsealed hydrate-bearing sediments after reservoir reformation in a large-scale simulator. Fuel 308, 121957. https://doi.org/10.1016/j.fuel.2021.121957.
Sun, Z., Li, N., Jia, S., et al., 2019. A novel method to enhance methane hydrate exploitation efficiency via forming impermeable overlying CO_2 hydrate cap. Appl. Energy 240, 842–850. https://doi.org/10.1016/j.apenergy.2019.02.022.
Tang, L., Li, X., Feng, Z., et al., 2007. Control Mechanisms for gas hydrate production by depressurization in different scale hydrate reservoirs. Energy Fuel 21 (1), 227–233. https://doi.org/10.1021/ef0601869.
Waite, W.F., Santamarina, J.C., Cortes, D.D., et al., 2009. Physical properties of hydrate-bearing sediments. Rev. Geophys. 47 (4), 1–38. https://doi.org/10.1029/2008RG000279.
Waite, W.F., Winters, W.J., Mason, D.H., 2004. Methane hydrate formation in partially water-saturated Ottawa sand. Am. Mineral. 89 (8–9), 1202–1207. https://doi.org/10.2138/am-2004-8-906.
Wang, B., Fan, Z., Wang, P., et al., 2018. Analysis of depressurization mode on gas recovery from methane hydrate deposits and the concomitant ice generation. Appl. Energy 227, 624–633. https://doi.org/10.1016/j.apenergy.2017.09.109.
Wang, Y., Li, X., Xu, W., et al., 2013. Experimental investigation into factors influencing methane hydrate formation and a novel method for hydrate formation in porous media. Energy Fuel 27 (7), 3751–3757. https://doi.org/10.1021/ef400720h.
Wang, Y., Wang, L., Li, Y., et al., 2020. Effect of temperature on gas production from hydrate-bearing sediments by using a large 196-L reactor. Fuel 275, 117963. https://doi.org/10.1016/j.fuel.2020.117963.
Winters, W.J., Pecher, I.A., Waite, W.F., et al., 2004. Physical properties and rock physics models of sediment containing natural and laboratory-formed methane gas hydrate. Am. Mineral. 89 (8–9), 1221–1227. https://doi.org/10.2138/am-2004-8-909.
Xiao, C., Li, X., Li, G., et al., 2022. Numerical analysis of production behaviors and permeability characteristics on the second gas hydrate production test in the South China Sea. Energy Fuel 36 (18), 10960–10974. https://doi.org/10.1021/acs.energyfuels.2c02385.
Xu, Z., Hu, T., Pang, X., et al., 2022. Research progress and challenges of natural gas hydrate resource evaluation in the South China Sea. Pet. Sci. 19 (1), 13–25. https://doi.org/10.1016/j.petsci.2021.12.007.
Yamamoto, K., Terao, Y., Fujii, T., et al., 2014. Operational overview of the first offshore production test of methane hydrates in the Eastern Nankai Trough. Offshore Technology Conference Houston, Texas, USA. OTC-25243-MS. https://doi.org/10.4043/25243-MS.
Yamamoto, K., Wang, X.X., Tamaki, M., et al., 2019. The second offshore production of methane hydrate in the Nankai Trough and gas production behavior from a heterogeneous methane hydrate reservoir. RSC Adv. 9 (45), 25987–26013. https://doi.org/10.1039/c9ra00755e.
Ye, J., Qin, X., Xie, W., et al., 2020. The second natural gas hydrate production test in the South China Sea. Chin Geol. 3 (2), 197–209. https://doi.org/10.31035/cg2020043.
Yin, Z., Linga, P., 2019. Methane hydrates: a future clean energy resource. Chin. J. Chem. Eng. 27 (9), 2026–2036. https://doi.org/10.1016/j.cjche.2019.01.005.
Yuan, Q., Sun, C., Wang, X., et al., 2013. Experimental study of gas production from hydrate dissociation with continuous injection mode using a three-dimensional quiescent reactor. Fuel 106, 417–424. https://doi.org/10.1016/j.fuel.2012.12.044.
Zhao, E., Hou, J., Liu, Y., et al., 2020. Enhanced gas production by forming artificial impermeable barriers from unconfined hydrate deposits in Shenhu area of South China sea. Energy 213, 118826. https://doi.org/10.1016/j.energy.2020.118826.

Zhao, J., Fan, Z., Dong, H., et al., 2016. Influence of reservoir permeability on methane hydrate dissociation by depressurization. Int. J. Heat Mass Tran. 103, 265–276. https://doi.org/10.1016/j.ijheatmasstransfer.2016.05.111.

Zhao, J., Liu, D., Yang, M., et al., 2014. Analysis of heat transfer effects on gas production from methane hydrate by depressurization. Int. J. Heat Mass Tran. 77, 529–541. https://doi.org/10.1016/j.ijheatmasstransfer.2014.05.034.

Zhu, Y., Yang, X., Huang, X., et al., 2024. Acoustic characterization of hydrate formation and decomposition in clay-bearing sediments. Pet. Sci. 21 (4), 2830–2838. https://doi.org/10.1016/j.petsci.2024.06.008.